



# 1 Hyperspectral mapping of density, porosity, stiffness, and strength in

# 2 hydrothermally altered volcanic rocks

- 3 Samuel T. Thiele<sup>1</sup>, Gabor Kereszturi<sup>2</sup>, Michael J. Heap<sup>3,4</sup>, Andréa de Lima Ribeiro<sup>1</sup>, Akshay Kamath<sup>1</sup>,
- 4 Maia Kidd<sup>2</sup>, Matías Tramontini<sup>5</sup>, Marina Rosas-Carbajal<sup>6</sup>, Richard Gloaguen<sup>1</sup>
- 6 <sup>1</sup>Helmholtz-Zentrum Dresden-Rossendorf, Helmholtz Institute Freiberg, Chemnitzer Str. 40, 09599 Freiberg, Germany
- 7 <sup>2</sup>Volcanic Risk Solutions, School of Agriculture and Environment, Massey University, Palmerston North, New Zealand
- 8 <sup>3</sup>Université de Strasbourg, CNRS, Institut Terre et Environnement de Strasbourg, UMR 7063, 5 rue Descartes, Strasbourg
- 9 F-67084, France
- 10 <sup>4</sup>Institut Universitaire de France (IUF), Paris, France
- 11 <sup>5</sup>CONICET Facultad de Ciencias Astronómicas y Geofísicas, Universidad Nacional de La Plata, Argentina
- 12 <sup>6</sup>Université de Paris Cité, Institut de Physique du Globe de Paris, CNRS, F-75005 Paris, France
- **13** *Correspondence to*: Samuel T Thiele (s.thiele@hzdr.de)

14 Abstract. Heterogeneous structures and diverse volcanic, hydrothermal, and geomorphological processes hinder the 15 characterisation of the mechanical properties of volcanic rock masses. Laboratory experiments can provide accurate rock 16 property measurements, but are limited by sample scale and labor-intensive procedures. In this contribution, we expand on 17 previous research linking the hyperspectral fingerprints of rocks to their physical and mechanical properties. We acquired a 18 unique reflectance dataset covering the visible-near infrared (VNIR), shortwave infrared (SWIR), midwave infrared 19 (MWIR), and longwave infrared (LWIR) of rocks sampled on eight basaltic to andesitic volcanoes. We trained several 20 machine learning models to predict density, porosity, uniaxial compressive strength (UCS), and Young's modulus (E) from 21 the spectral data. Significantly, nonlinear techniques such as multilayer perceptron (MLP) models were able to explain up to 22 80% of the variance in density and porosity, and 65–70% of the variance in UCS and E. Shapley value analysis, a tool from 23 explainable AI, highlights the dominant contribution of VNIR-SWIR features that can be attributed to hydrothermal 24 alteration and MWIR-LWIR features witnessing volcanic glass content and, likely, fabric and/or surface roughness. These 25 results demonstrate that hyperspectral imaging can serve as a robust proxy for rock physical and mechanical properties, 26 offering an efficient, scalable method for characterising large areas of exposed volcanic rock. The integration of these data 27 with geomechanical models could enhance hazard assessment, infrastructure development, and resource utilisation in 28 volcanic regions.





#### 30 1 Introduction

31 Society is dependent on subsurface resources, including groundwater (Foster et al., 2013), low-carbon energy (Lund and 32 Toth, 2021; Soltani et al., 2019) and critical raw materials (Lewicka et al., 2021). Simultaneously, population growth and 33 increasingly extreme weather (Aubry et al., 2022; Farquharson et al., 2015) expose a growing number of people to 34 geological hazards, including rock falls, landslides, and volcanic eruptions. Effective management of these resources and 35 hazards requires detailed characterisation of the subsurface geology, its physical properties (e.g., density and permeability), 36 and its mechanical behaviour (e.g., strength and deformability). 37 Volcanic regions commonly host mineral, water, and geothermal resources, and are also extremely prone to geological 38 hazards. However, the mechanical behavior of volcanic rock masses remains challenging to characterize, due to the diverse 39 volcanic, hydrothermal, sedimentological and geomorphological processes that shape and reshape them (Heap and Violay, 40 2021). Although mechanical properties can be accurately and routinely measured in the laboratory, samples are typically 41 limited to the centimeter- to decimeter-scale, which is several orders of magnitude smaller than is required to predict surface 42 deformation or reservoir behavior. Obtaining sufficient measurements to statistically characterize large-scale mechanical 43 variability thus remains a challenge, given the laborious mechanical tests required to measure e.g., strength, stiffness, and 44 hydraulic properties. 45 Several proxy measures have been developed to help mitigate sampling limitations, including field measurements of porosity 46 and permeability (Farguharson et al., 2015; Mordensky et al., 2018), Schmidt hardness (del Potro and Hürlimann, 2009; 47 Dincer et al., 2004; Harnett et al., 2019; Mordensky et al., 2018), point-load strength (Poganj et al., 2025), reflectance 48 spectroscopy (Bakun-Mazor et al., 2024; Kereszturi et al., 2023; Schaefer et al., 2021), and thermal inertia (Franzosi et al., 49 2023; Loche et al., 2021; Mineo and Pappalardo, 2016). These proxies are easier to obtain than many mechanical test results, 50 and often correlate well with important laboratory-measured properties like strength and stiffness after calibration for 51 specific geological contexts or settings. 52 Hyperspectral reflectance data could provide an especially useful proxy for mechanical properties, as they can be collected 53 rapidly and, potentially, acquired remotely using imaging sensors. This approach could make use of the latent influence that 54 lithological properties like mineralogy, fabric, and porosity have on both the hyperspectral and mechanical response. For 55 instance, Schaefer et al. (2021) used visible-near (VNIR; 350–900 nm) and shortwave (SWIR; 900–2500 nm) infrared 56 reflectance spectroscopy to correlate spectral features and mineralogy with porosity and strength, and identified moderate 57 Spearman rank correlation with 390, 2207, and 2325 nm features. Kereszturi et al. (2023) also used VNIR and SWIR 58 hyperspectral data to predict porosity and unconfined compressive strength (UCS) in volcanic rocks, explaining 40–50% of 59 the mechanical variance. Lee et al. (2023) applied VNIR, SWIR, and midwave infrared (MWIR; 3000-5200 nm) data to 60 predict the dynamic elastic moduli of finely laminated shales, with R<sup>2</sup> scores between 0.4 and 0.8, but across a small sample 61 set. Most recently, Bakun-Mazor et al. (2024) used VNIR-SWIR and longwave infrared (LWIR; 7000–12000 nm) spectra to 62 estimate several mechanical properties, including UCS, in carbonate rocks, with generally high (0.8 to 0.9) R<sup>2</sup> scores.





- 63 However, further research is needed to understand the relationships between hyperspectral data and the mechanical
- 64 properties of volcanic rocks, due to their complex microstructures and mineralogies, as well as the impact of hydrothermal
- 65 alteration.
- 66 In this contribution we investigate the relationships between hyperspectral data and the mechanical properties of volcanic
- 67 rocks, specifically focusing on density, porosity, UCS, and Young's modulus (E). E is of particular interest, as it has not
- 68 previously been linked to hyperspectral data and is crucial to predict surface deformation occurring during e.g. construction
- 69 or tunnelling works, mining, and volcanic unrest (Arens et al., 2022; Harnett and Heap, 2021; Heap et al., 2020b, 2021b;
- 70 Hickey et al., 2022; Hoek and Diederichs, 2006; Strehlow et al., 2015; Vrakas et al., 2018).
- 71 We therefore expanded the dataset presented by Kereszturi et al. (2023) to include samples from more volcanoes, and cover
- 72 an extended spectral range (VNIR-SWIR-MWIR-LWIR). This dataset is then leveraged to:
- 73 1. Train machine learning models to predict density, porosity, UCS, and E.
- 74 2. Identify hyperspectral indicators for hydrothermal alteration, and explore how these are linked to the measured and predicted mechanical properties.
- 76 3. Quantify the influence of different spectral ranges on each predicted property, to explore the spectral features that inform our model.
- 78 By advancing our understanding of the correlations between hyperspectral and mechanical properties, we ultimately aim to 79 improve our ability to characterise complex and heterogeneous volcanic rock masses.

## 80 2 Theory

# 81 2.1 Light-matter interactions: reflection and scattering

- 82 Light-matter interactions are complex, and governed by multiple interacting optical phenomena. Reflectance is a remotely
- 83 measurable, dimensionless expression of these interactions, defined by the ratio between the excitation signal (illumination
- 84 or irradiance, W.m-2) and signals emitted back towards a sensor (radiance, W.m-2.sr-1). Hyperspectral sensors measure this
- 85 returned radiance, and split it into many narrow but contiguous wavelength ranges to derive a radiance spectra that, after
- 86 correction to derive reflectance, contains information on the target material.
- 87 Links between hyperspectral reflectance spectra and mineralogy are well established, as reviewed by Laukamp et al. (2021)
- 88 and Williams and Ramsey (2024). Specific spectral ranges can be used to identify certain elements, due to the absorption of
- 89 VNIR range light during electronic transitions in metals like Fe, and covalent bonds that absorb energy at specific
- 90 wavelengths by stretching and bending activity. Compounds containing O-H, C-O and S-O bonds tend to have diagnostic
- 91 absorption features in the SWIR and MWIR ranges, while stretching and bending vibrations of Si-O bonds cause absorption
- 92 in the upper MWIR and LWIR ranges.
- 93 In volcanic contexts, electronic transition absorptions in the VNIR range can be used to detect common Fe3+ and Fe2+ rich
- 94 minerals, including hematite, goethite, and jarosite. SWIR range data are sensitive to hydroxylated silicates, including clay





95 minerals, sulphates, and carbonates. The MWIR range is less widely used, but also includes diagnostic absorption features 96 for hydroxylate silicate and carbonate minerals. Finally, the upper MWIR and LWIR range is strongly influenced by 97 absorptions from the Si-O bonds in silicate minerals and glasses, and can be used to characterise the extent of silica 98 polymerization and to identify most rock-forming silicates (e.g., quartz, feldspars, pyroxene). 99 Regardless of the spectral range, features observed in reflectance spectra are determined by a combination of refraction, 100 absorption and scattering characteristics inherent to each material, and abide by Snell's law (Kirkland et al., 2003; Rost et al., 101 2018). The expected positions of absorption features are well-established, including subtle variations caused by differences 102 in crystal structure that often allow precise identification of specific minerals (Laukamp et al., 2021). However, spectral 103 characteristics like overall albedo, broad fluctuations in reflectance intensity, and the depth and asymmetry of absorption 104 modes (spectral contrast), can vary significantly between rocks with the same mineralogy. These wavelength-dependent 105 variations derive from processes occurring as light interacts with the surface of a rock and while traveling through its solid 106 constituents (and pore spaces), carrying information linked to surface and bulk physical properties. For consistency, we refer 107 to changes in the direction and intensity of light which are directly dependent on the surface characteristics as 'surface 108 scattering', and as 'volume scattering' when these changes are linked to processes occurring below the surface. Accordingly, 109 light-matter interactions in natural minerals can be understood through the combination of two optical scattering 110 components: surface and volume (Osterloo et al., 2012; Rost et al., 2018; Vincent and Hunt, 1968). 111 Surface scattering occurs when light interacts mostly with the superficial layer of a mineral, which acts as a mirror-like 112 interface and reflects light without transmitting it to the internal constituents of a rock (hereafter referred to as grains, 113 although we use this term inclusively of crystals, clasts and fragments) (Fig. 1a). This happens when the extinction 114 coefficient of light in a medium (k) is larger than its refractive index (n); as most of the incident radiation is absorbed at the 115 surface and not transmitted to higher depths (Hardgrove et al., 2016). The magnitude of surface scattering can vary with 116 wavelength (as n and k are both wavelength dependent), and is highly sensitive to the scale of surface topography relative to 117 the wavelength (Rayleigh's criterion; Hapke, 2012, 1981). A surface is considered perfectly smooth when its average 118 roughness is smaller than the wavelength of the incident light, with the outcoming light being reflected at the same angle as 119 the incoming radiation. This phenomenon, known as specular reflection, is particularly important in the LWIR region 120 (5,000-50,000 nm) (Fig. 1a). As roughness increases, surface irregularities serve as points for the incoming light to scatter 121 into several directions, spreading the total reflected energy in a Lambertian-like process known as diffuse scattering (Fig. 122 1a). Diffuse scattering is particularly important in the VNIR-SWIR analysis of rough surfaces in which asperities are 123 oriented towards different directions. In extreme cases, multiple diffuse patterns can occur within a small area, leading to a 124 multi-path scattering pattern (Fig. 1a). 125 In addition to impacting surface scattering, increased roughness enhances the transmission of incoming light through grains 126 at the sample surface, even when k is larger than n. This process, known as volume scattering, introduces longer paths and 127 changes in direction for light travelling within the medium leading to partial energy loss and reduced spectral contrast 128 (Kirkland et al., 2003, 2001; Osterloo et al., 2012; Rost et al., 2018) due to light undergoing absorption within the medium





129 prior to being scattered back to the surface (Fig. 1d). Increased volume scattering is also linked to the grain size, and 130 observed especially in the presence of smaller grains (Hunt and Vincent, 1968; Lyon, 1965; Mustard and Hays, 1997; 131 Salisbury and Wald, 1992). It is important to note that although the impact of volume scattering on the reflectance spectrum 132 is dependent on the inherent optical properties of the mineral, roughness, and the wavelength of the incoming light, these 133 relationships are highly non-linear and difficult to characterise for real multi-phase materials (i.e. rocks). In the LWIR, both 134 increased and decreased spectral contrast have been associated with volume scattering, highlighting the complexity of these 135 interactions (Osterloo et al., 2012). 136 For most real materials and mineral mixtures, both surface and volume scattering influence the reflectance spectra, with 137 different contributions depending (again) on the surface roughness, grain size, and wavelength range. An exemplary case of 138 surface and volume processes acting simultaneously is encountered for porous materials (Fig 1e). Pore size, shape and 139 distribution are directly linked to surface roughness, impacting the light-matter interaction dynamics by: i) enhancing the 140 volume scattering by transmitting light through interfaces barriers with different k and n (e.g. mineral/air/mineral interfaces), 141 leading to longer travel paths; and ii) by trapping light at pores with high depth-to-width ratios, causing multiple surface 142 reflection paths (cavity effect) and, in extreme cases, leading to total absorption of light before it can be reflected out of the 143 cavity (Hardgrove et al., 2016; Huang et al., 2021; Kirkland et al., 2001). Ultimately, increased porosity may lead to 144 important changes in the reflectance spectrum, particularly in the thermal region (5,000–50,000), and is associated with 145 reduced spectral contrast and inhibition of diagnostic mineralogical absorption features (Osterloo et al., 2012; Rost et al., 146 2018; Salisbury and Eastes, 1985).

## 147 2.2 Hapke's model

148 Hyperspectral cameras operate as fixed-position external-reflectance sensors, collecting the radiation scattered in a specific 149 direction from a material excited by a light source of known characteristics. Hence, material properties which affect the 150 amount of radiation scattered towards a detector influence the measured spectra. Several models (broadly known as the 151 Hapke model) have been proposed to investigate these light-mineral interaction dynamics, initially in the context of 152 extraterrestrial remote sensing (Hapke, 2012, 2008, 2002, 1984, 1981). Hapke's models aim to estimate bidirectional 153 reflectance signals collected by external-reflectance sensors. They are based on radiative transfer theory and on the works 154 from Chandrasekhar (1960), and form an important theoretical basis for hyperspectral imaging applications. The core 155 premise of Hapke's models is that reflectance spectra can be parameterised as a function of material type and morphological 156 properties (Hapke, 1993).

157 While a detailed examination of Hapke's model(s) is beyond the scope of this contribution, we aim here to identify several 158 key elements that link reflectance signals with roughness, grain size and porosity. These effects are highlighted using the 159 following formula,





161 
$$r(i,e,\alpha,\lambda) = K \frac{\omega(\lambda)}{4} \left( [1 + B(\alpha)]P(\alpha) + M(i,e,\alpha,\lambda) - 1 \right),$$
162 
$$(1)$$

where  $r(i,e,\lambda)$  is the scattering intensity (radiance); K is the filling factor (linked to porosity; Hapke, 2008); ( $\lambda$ ) is the 164 average single scattering albedo (SSA; linked to absorption and scattering at particle level and dependent on the wavelength 165  $\lambda$ ); B() is the opposition surge function (Hapke, 1993, 1986); P() is the average single scattering function for the phase angle 166; i and e are the angles of incidence and emission; M(i,e,, $\lambda$ ) represents the wavelength-dependent multiple scattering effect 167 (MSE). It is important to note that Hapke's refers to 'scattering' as an integration of all radiation emitted by a surface 168 following interactions with an excitation source, with no distinction between surface and volume processes. Instead, the 169 models provide a holistic approach in which multiple terms are influenced by both surface and volume processes. In this 170 context, radiance is thus the total signal scattered by an object towards a detector. In hyperspectral remote sensing, the 171 distinction between surface and volume scattering contributions is important, as surface and subsurface rock characteristics 172 are linked to changes in the reflectance spectra (cf., section 2.1).

173

The single and multiple scattering terms (SSA and MSE) are the primary contributors to the reflectance estimated by the model. Whilst SSA represents the probability of light being scattered or absorbed by a single grain, MSE (derived from Ambartsumian-Chandrasekhar H-function and dependent on SSA) accounts for multiple scattering prior to its emission towards a detector. Both parameters are material-specific, and vary according to changes in roughness, grain size, and wavelength of light. Another core term is the phase function P(), which estimates how much light is scattered in a given direction relative to the direction of incoming light as a function of the angle between the illumination direction and the viewing direction (phase angle, ). The intensity and direction of the phase function are not material-specific, but also depends on roughness, grain size and wavelength. The opposition surge term B() is also linked to , and introduces a surface brightening effect as decreases (Hapke, 2002). Finally, the porosity parameter K accounts for changes in scattered signals due to increasing porosity and/or decreasing density (Hapke, 2008).

184

185 To summarise, Hapke's models provide an important tool to understand the link between hyperspectral reflectance spectra 186 and sample roughness, grain size, porosity and composition. It is based on radiative transfer theory and traditionally used to 187 describe the scattering of light by planetary surfaces. It estimates the bidirectional reflectance of a surface, considering both 188 single and multiple scattering of light. The model can be tuned for specific application, and generally incorporate parameters 189 such as single-scattering albedo, phase function, and surface roughness which have a direct impact on the bidirectional 190 reflectance signals. Hapke's model is therefore a strong basis for understanding the interaction of light with rock surfaces, 191 aiding in the interpretation of remote sensing data. While the complexity of real samples typically limits the model's 192 practical application, it provides a useful theoretical framework that will help us to understand and interpret hyperspectral 193 reflectance spectra.





194

#### 195 3 Methods

## 196 3.1 Sample database

197 For this study, we compiled a new database of individual, well-characterised core samples that have been subjected to 198 laboratory rock deformation experiments (Heap et al., 2021a, 2020a; Leiter et al., 2024; Schaefer et al., 2023; Tramontini et 199 al., 2025; Vairé et al., 2024). These samples were collected in the scope of previous studies from basaltic to rhyolitic 200 composite volcanoes, including Cracked Mountain (Canada; Leiter et al., 2024), Ruapehu (New Zealand; Schaefer et al., 201 2023), La Soufrière de Guadeloupe (Eastern Caribbean; Heap et al., 2021b, 2021a), Ohakuri (New Zealand; Heap et al., 202 2020a), Chaîne des Puys (France; Vairé et al., 2024), Copahue (Argentina/Chile; Tramontini et al., 2025), Tongariro (New 203 Zealand; Kidd et al., 2025), and Whakaari (New Zealand; Kidd et al., 2025).

204 Most of the sampled rocks are basaltic to andesitic in composition, and cover a range of textures (breccias, pyroclastic, and 205 coherent lava rocks). A breadth of hydrothermal alteration is also covered, ranging from dominantly fresh rocks (e.g., from 206 Chaîne des Puys; Vairé et al., 2024) through to intense hydrothermal alteration (e.g., some samples from Ruapehu and 207 Whakaari; Schaefer et al., 2023). Altered samples in our sample set were subject to acid-sulphate related mineralogical 208 changes, including the formation of sulphates (e.g., jarosite, alunite and anhydrite), phyllosilicates (e.g., kaolinite and 209 montmorillonite), and various polymorphs of quartz (Heap et al., 2021a; Kereszturi et al., 2020). This diversity of alteration 210 is intended to help our machine learning models to learn some of the alteration systematics and capture how these can 211 influence the physical and mechanical properties of volcanic rocks.

#### 212 3.2 Laboratory testing

213 Mechanical test cores were prepared with a diameter of 20 mm and a length of ca. 40 mm. Measurements and experiments 214 were either performed at University of Strasbourg (France) or University of Canterbury (New Zealand). Prior to testing, the 215 samples were dried in a vacuum oven at 40 °C for a minimum of 48 hours (Strasbourg) or oven-dried at 60 °C for a 216 minimum of 48 hours (Canterbury). Dry bulk density was calculated using the dry mass and bulk volume of each sample. 217 Connected porosity was calculated using the skeletal volume, measured using an AccuPyc II 1340 pycnometer (Strasbourg 218 and Canterbury), and the bulk volume of each sample. 219 Uniaxial compressive strength (UCS) experiments were performed using a uniaxial load frame supplied by Schenk 220 (Strasbourg) or a 3000 kN Technotest uniaxial load frame (Canterbury). All experiments were performed on dry samples at 221 ambient laboratory temperatures. Samples were deformed at a constant strain rate of 10–5 s–1 until macroscopic sample 222 failure (Fig. 2a). Axial displacement and axial force were measured by a linear variable differential transducer and a load 223 cell, respectively, and were converted to axial strain and axial stress using the initial length and radius of the sample,





224 respectively. More information, as well as schematic diagrams of the devices, can be found in Heap et al. (2014) and

225 Mordensky et al. (2018).

226 First, the maximum stress of each loading curve was identified as the UCS. The pre-failure loading curve was then smoothed

227 slightly using a Savitzky-Golay filter and resampled to regular stress increments using a linear interpolation. The slope of

228 the most linear part of the resampled loading curve was then identified to calculate E, using the random sample and

229 consensus (RANSAC) algorithm. This regression technique robust to outliers iteratively fits data with a function (in this case

230 a linear) using random minimal subsets (two points) and maximises the number of inliers within a threshold distance. This

231 approach successfully identifies the linear part of each loading curve while remaining robust to outliers caused by pre-failure

232 inelastic deformation by maximising the number of inliers (rather than minimising residuals as per e.g., least-squares

233 regression, Fig. 2c), allowing robust and objective measurement of E.

234

## 235 3.3 Hyperspectral data acquisition

236 A total of 332 individual core samples were compiled from eight basaltic to andesitic volcanoes and arranged on

237 non-reflective sample trays (Fig. 2a). These samples were grouped by size to limit focal blur, fixed in place using plasticine

238 and leveled to reduce illumination artifacts. Each tray was then scanned using a Specim SiSuROCK drill core scanner, which

239 contains Specim AisaFENIX, FX50 and AisaOWL hyperspectral sensors and a high spatial Specim RGB-Jai camera (Fig.

240 2b). The workflow described by Thiele et al. (2024) was used to coregister data from each of the sensors and to convert from

241 measured radiance to relative reflectance.

242 Each sample was then extracted from the coregistered stack of hyperspectral (and RGB) imagery using napari-hippo (Thiele

243 et al., 2024), and stored as a separate set of images. The spectra of each image was smoothed slightly with a Savitzky-Golay

244 filter (using a 1st order polynomial and window size of 5 bands), and hull-corrected using hylite (Thiele et al., 2021) to

245 amplify spectral absorption features and reduce illumination artifacts caused by non-planar sample geometries. VNIR to

246 MWIR spectra were corrected using an upper hull correction, while a lower hull correction was applied to the LWIR range

247 data.

248 Median spectra from each mechanical test sample were then compiled into a spectral library covering the

249 VNIR-SWIR-MWIR-LWIR range. These were combined with the corresponding mechanical property measurements to

250 derive a training dataset.

251 Their mineralogy was characterised by indices extracted from the spectra of each sample using the minimum wavelength

252 mapping approach (van der Meer et al., 2018) implemented in hylite (Thiele et al., 2021). These indices (Table 1) quantify

253 specific spectral absorptions resulting from vibrational and bending vibrations associated with water, sulfate, hydroxylated

254 phyllosilicates, and silicate minerals (Laukamp et al., 2021; Schodlok et al., 2016). Two composite indices were also

255 calculated, to characterize bulk-composition and the extent of hydrothermal alteration. The first is the Mafic-Felsic Index of

256 Schodlok et al., (2016), which distinguishes samples with basaltic compositions from those that are more evolved. This





257 index, hereafter referred to as MFI, was computed by applying a lower-hull correction to the LWIR spectra between 7640

258 and 10620 nm and identifying the general position (wavelength) of the reflection peak within this range, using the

259 polynomial fitting approach implemented in hylite (Thiele et al., 2021). The results were then normalized to range between 0

260 (maxima at 10620 nm, indicating mafic compositions) and 1 (maxima at 7640 nm, indicating felsic compositions).

261 The second bulk index was derived by averaging the H2O and OH absorptions at ~1900 and 1400 nm (Table 1), to track the

262 total amount of water (as H2O, in e.g. quartz-hosted fluid inclusions, and as -OH groups in e.g., clay minerals). Because

263 most of the measured volcanic rocks are initially dry (with some exceptions, e.g., phreatomagmatic tuff), this water often

264 indicates hydrothermal alteration. We thus use this index as a rough proxy for hydrothermal alteration (and weathering)

265 processes. The presence of hydrated (alteration) minerals has been shown to correlate with mechanical response (Heap et al.,

266 2022).

267

## 268 3.4 Regression models

269 Each target variable (density, porosity, UCS, and E) requires transformation prior to model fitting, to reduce skew (Fig. 3)

270 and ensure the back-transformed predictions are correctly scaled (non-negative and, in the case of porosity, between 0 and 1).

271 A square root transform (Fig. 3e) was found to perform better than a log-transform (Fig. 3f), likely as it resulted in more

272 normally distributed data. Porosity was converted to a ratio of voids to solids (1 - porosity) prior to the square root transform,

273 mitigating challenges fitting regressions to closed data.

274 We ensure a robust calibration/validation by defining five folds using a stratified split with respect to porosity, to ensure that

275 each fold contains diverse mechanical properties. Several machine learning approaches (lasso regression, partial least square

276 regression, support vector regression, and multilayer perceptron regression), known to be adapted to this genre of tasks,

277 were then evaluated using the R2 metric and 5-fold cross validation (to account for potential overfitting). Model

278 hyperparameters were optimised to maximise the training R2 score, as documented in the Jupyter notebooks included in the

279 supplementary material. Finally, the best models were combined into an ensemble, allowing the prediction variance to be

280 used as a measure of uncertainty.

#### 281 3.5 SHAP analysis

282 Shapley values (Shapley, 1973) have recently been adapted to help understand the predictions made by deep learning

283 models. Based on cooperative game theory, Shapley values quantify the contribution of individual features to output

284 predictions, providing a theoretically grounded measure of the average marginal contribution of each input feature across all

285 possible feature subsets (Lundberg and Lee, 2017). This allows a more detailed interpretation than other explanation

286 approaches, and in this case helps link model predictions to specific hyperspectral bands.

287 We used the python package SHAP (Shapley Additive Explanations; Lundberg and Lee, 2017) to compute Shapley values

288 for our ensemble models. Due to the various types of models included in these ensembles, a stochastic estimation approach





289 (KernelSHAP) was used. KernelSHAP is a model-agnostic algorithm that estimates Shapley values by systematically 290 perturbing input variables and measuring the resulting changes. The perturbative nature of this algorithm makes it 291 computationally expensive, requiring us to compute Shapley values only for a subset of our test dataset. This subset was 292 selected using k-means clustering, such that 16 representative data points (cluster centroids) could be selected for use by the 293 Kernel Explainer.

296 A comparison of MFI, a proxy for composition, and hydration index, a proxy for hydrothermal alteration, highlights the 297 spectral diversity of our dataset (Fig. 4). Two broad populations of basalt (lower) and andesite (upper) form clear horizontal

#### 294 4 Results

## 295 4.1 Spectral response of hydrothermal alteration

298 "bands", each of which contains variable amounts of hydration. The MFI results broadly match the expected composition of 299 each volcano, albeit with exceptions including two altered samples from Whakaari with anomalously low MFI (due to the 300 confounding influence of non-silicate alteration minerals like jarosite or sulphur, rather than a mafic composition). 301 Diagnostic absorption features for kaolinite ( $v+\delta M2OHo$ ) and other clay minerals ( $v+\delta(A1)-OH$  and  $v+\delta(Mg)-OH$ ) are 302 prominent in many altered samples. Of these, the kaolinite-rich samples (Fig. 4e) tended to be associated with deeper 2vSi-O 303 absorptions in the MWIR range (at  $\sim$ 4500 nm and indicative of silicification) or  $\delta$ S-O absorptions in the SWIR range (at 304 ~1750 nm), indicating silicification and/or the presence of sulphate minerals like jarosite and alunite. In combination, these 305 spectral features indicate advanced argillic alteration, and are mostly associated with higher (andesitic) values of MFI (as our 306 dataset currently lacks basaltic examples of advanced argillic alteration). 307 Many samples also contain well defined  $v+\delta(A)$ -OH absorption features (Fig. 4a), but without the previously mentioned 308 kaolinite, sulphate, or quartz-related absorption features. These are indicative of illite and smectite group clay minerals 309 formed by lower-temperature (<120° C) and/or higher pH hydrothermal alteration or weathering. Many of the basaltic 310 samples (lower MFI) also contain distinctive  $v+\delta(Mg)OH$  absorption features at 2300 nm, while lacking the  $v+\delta(Al)-OH$ 311 feature (Fig. 4b). We interpret this as either primary Al-poor clays (e.g., in palagonite tuffs), or as the result of argillic 312 alteration or weathering in Al-poor primary lithologies to form Fe- and Mg- rich clay minerals, like nontronite and hectorite. 313 Notably, all samples with spectral absorptions indicative of hydrothermal alteration also had prominent vOH and 314 vOH+ $\delta$ H2O absorptions at ~1400 and 1900 nm. This suggests that these combined features (our hydration index) can be 315 used to broadly quantify the intensity of hydrothermal alteration, because primary volcanic lithologies tend not to contain 316 hydrated or hydroxylated phases. Samples with higher hydration indices tended to be less dense (Fig. 5a) and have lower 317 UCS and E (Fig. 5c-d) than counterparts with lower hydration indices. Porosity showed a more complex relationship to the 318 hydration index (Fig. 5b), with a distinctive set of highly porous but non-hydrated samples (vesiculated lavas), and highly 319 porous and hydrated samples.





## 320 4.2 Rock property prediction

321 The tested machine learning models gave a wide range of prediction accuracies, with highly varied 5-fold cross-validation 322 R2 scores (Table 2). Linear models (PLSR and Lasso) performed poorly, suggesting a highly non-linear relationship between 323 spectral response and rock properties (Table 2). Support Vector Regression (SVR) and Multilayer Perceptron (MLP) models 324 were able to learn the nonlinear relations, yielding 5-fold cross validated R2 scores between 0.5 and 0.85 for each of the rock 325 properties. Deeper multilayer perceptrons (with 8 to 16 fully connected layers) performed best. The need for depth further 326 emphasises the need to capture nonlinear links in the underlying data structure and modelling.
327 Models fit to principal component (PCA) transformed inputs (retaining 25 independent features), including the MLP models 328 that theoretically work well with high-dimensionality input, performed better than models fit directly to concatenated 329 spectra.
330 No substantial difference in accuracy was observed between MLP models predicting a single output (i.e. univariate MLP 331 models that predict a single rock property) and multivariate MLP models (that predict each of the four rock properties 332 together). Ensemble predictions computed by averaging outputs from a set of nine manually selected (best-performing) SVM 333 and MLP models show similar or slightly improved R2 scores (relative to the individual models). However, these ensemble 334 models allow an estimate of prediction uncertainty (Fig. 6), based on the standard deviation (σ) of the individual model

337 380 MPa), and over-estimated E for several samples from Ruapehu and Whakaari.
338 Interestingly, models trained and tested on the basaltic samples achieved higher R2 scores than equivalents trained and tested
339 on andesitic ones (Table 2). This implies that the rock properties of basalts (in our dataset) were easier to predict than
340 andesites, possibly due to the variability of the hydrothermally altered andesite relative to the basalts (which were mostly
341 fresh or palagonitized).

335 predictions. In most cases the measured rock property was within  $2\sigma$  of the ensemble mean, though several notable outliers 336 can also be identified. These include the prominently under-predicted UCS for one sample from Ruapehu (156 rather than

#### 342 4.3 Important spectral ranges

Shapley values calculated for our ensemble predictions were aggregated to explore the contribution of each spectral range (Fig. 7). The results suggest the VNIR-SWIR range contributes most to predictions of density, UCS, and E that are below the expected (average) prediction, while the LWIR range makes a substantial contribution for above-average predictions. The opposite can be seen for porosity, where VNIR-SWIR bands mostly drive above average predictions. This indicates that the models learn to associate SWIR-active alteration minerals with reduced UCS, E, and density (and associated porosity increase).

349 Per-band Shapley values can also constrain the specific spectral features that, in combination, contribute to each prediction.

350 To reduce the influence of lithological effects, these per-band Shapley values were calculated for models trained only on the

351 basaltic and andesitic subsets (Fig. 8). The results highlight a sensitivity to spectral ranges matching the expected





352 mineralogical absorptions, though it is striking that the informative bands tend to occur on the absorption "shoulders" rather 353 than their centres (Fig. 8).

Strongly negative Shapley values are associated with 1800, 1900, and 2200 nm bands, which contain absorptions characteristic of hydrothermal alteration minerals (Table 1) for samples with low predicted E. Higher predictions also appear driven by these same bands, presumably due to an absence of absorption features in these wavelengths for these samples. In the MWIR, features at ~3400 and between 4200 and 4900 nm appear important, with several "doublets" (spectrally adjacent high and low Shapley values) indicating a sensitivity absorption shape (asymmetry) or position. The first of these bands (3400 nm) is likely related to v2HOH absorptions (though will have been quite distorted by the hull correction applied during pre-processing). The latter bands (4200–4900) are interpreted to relate to 2vSi-O absorptions from silicate minerals or 2vS-O absorptions from sulphates (Laukamp et al., 2021), though the last of these (4900) may also have been shifted by the

362 hull correction.
363 Notably, many more VNIR, SWIR, and MWIR bands appear important for predictions made by the andesitic model than the 364 basaltic one, presumably due to the more complex mineralogy of these samples. Informative bands in the LWIR range 365 between 8500 and 11000 nm and also likely relate to vSiO absorptions, though the mixtures of silicate minerals and glassy 366 matrix make these difficult to interpret specifically (Laukamp et al., 2021; Leight et al., 2024; Williams and Ramsey, 2024).

367 Informative bands for the andesite model are lower wavelength (8500–9200 nm) than those for the basaltic model

368 (8800–9800 nm), corroborating the change in silica polymerization between these sample sets.

## 369 5 Discussion

Our five-fold cross validated ensemble predictions show that hyperspectral data can be used to explain ~80% of the variance in density and porosity and 65–70% of the variance in strength (UCS) and Young's modulus (E), at least for the investigated basaltic and andesitic volcanic lithologies. The rapid acquisition and imaging abilities of hyperspectral sensors could thus be leveraged to better characterise complex volcanic rock masses, by extending laborious rock property measurements across large datasets from point spectrometers, hyperspectral core scanners and, potentially, outcrop hyperclouds (e.g., Thiele et al., 2024, 2022). The resulting thousands to millions of (ideally spatially continuous) property estimates would allow robust characterisation of the variability in volcanic rock matrix properties and, if combined with digitally mapped fracture information, provide some of the information needed to numerically predict larger-scale rock-mass properties (e.g., Cundall 188 et al., 2008).

## 379 5.1 Predicting density and porosity

380 Our predictions of density and porosity were remarkably accurate (5-fold CV R2 score of 0.81 and 0.84 respectively), 381 especially given the complex volcanic processes that influence these properties (vesiculation, pyroclastic processes, 382 alteration, and fracturing). Interestingly, linear methods such as LASSO and PLSR predicted density and porosity poorly





383 (Table 2), while the non-linear methods (MLP and SVR) achieved R2 scores >0.8. This suggests an inherently non-linear 384 relationship between reflectance, density, and porosity. The high accuracies of the non-linear models also indicate that they 385 are able to learn more than just the link between the hyperspectral data and mineralogy, as composition alone is expected to 386 be a poor predictor of porosity (Pola et al., 2012). We thus suggest that the hyperspectral data contain information on 387 porosity and density via the sensitivity of volume and surface scattering processes to pores at or near the sample's surface 388 (Fig. 1). As described by the Hapke model, such wavelength-dependent scattering effects are likely especially relevant for 389 longer wavelengths, supporting the Shapley values that show the LWIR data contributed significantly to many predictions 390 (Fig. 7). Larger vesicles that approach the 1 to 2 mm spatial resolution of the sensors could also influence the spectra, via the 391 cavity effect (Fig. 1), especially in the LWIR infrared range (where they are expected to reduce reflectivity and increase the 392 emissivity). 393 Our Shapley values highlight the important role of MWIR and LWIR bands, especially for high-density and low-porosity 394 samples (Fig. 7). It is also striking that the VNIR-SWIR and LWIR ranges tend to be in opposition (cancelling each other 395 out) for less extreme predictions (Fig. 7), emphasising the importance of the broad spectral range 396 (VNIR-SWIR-MWIR-LWIR) covered by the dataset. The special attention our machine learning models appear to be giving 397 to the shoulders of mineralogical absorption features (rather than their minima, which are typically related to composition) is 398 also noteworthy. We tentatively suggest that this highlights the sensitivity of our models to the shape and asymmetry of 399 absorption features, properties that are more significantly influenced by surface reflection and volume scattering processes

## 401 5.2 Predicting uniaxial compressive strength and Young's modulus

400 that likely give crucial information on surface roughness, grain size, and porosity.

The lower, but still informative, predictive power of our models for UCS and E indicates a complex relationship between spectral response, porosity, density, and alteration-related weakening (Heap et al., 2020a, or possibly strengthening in the case of silicification; Heap et al., 2021a). These non-linear models can explain  $\sim$ 70% of the total variance, noting that the R2 scores are likely substantially reduced by a small number of outliers (Fig. 6). This result is consistent with the combined models of Kereszturi et al. (2023), in which externally measured porosity and VNIR-SWIR information (characterising alteration mineralogy) explained 80% of the variance in UCS. We suggest that externally measured porosity was needed by Kereszturi et al. (2023) due the lack of LWIR information, which limited their ability to directly predict porosity from the hyperspectral data (R2 = 0.4). Our dataset clearly did not have this limitation (Section 5.1), indirectly improving also our predictions of UCS.

411 Theoretical links between reflectance spectra and grain size properties could further influence our machine learning models, 412 although we are unable to distinguish these effects from the previously discussed sensitivity to porosity. We also speculate 413 that it is likely the model is learning to distinguish glass-rich (and hence stiff and brittle) samples from more crystallised 414 ones, based on their distinctive LWIR expression (Williams and Ramsey, 2024). The sensitivity to glass could explain the 415 broad informative wavelength range indicated by the Shapley values in the LWIR (Fig. 8).





416 The remaining (unpredicted) variance in UCS and E could be attributed to micro-fractures, which will serve to reduce E and

417 UCS (Griffiths et al., 2017; Swanson et al., 2020; Takemura et al., 2003) with negligible spectral effect. Such fractures could,

418 for example, explain overpredicted outliers in Figs. 6 and 8. Micro-fractures are less likely to explain cases where our model

419 makes under-predictions however, including the notable outlier in Fig. 6c where the predicted UCS is ~250 MPa too low.

# 420 5.3 Hyperspectral quantification of hydrothermal alteration

421 VNIR-SWIR hyperspectral data are particularly useful for identifying hydrothermal alteration, discriminating between

422 different alteration types, and vectoring towards mineral deposits (e.g., Cudahy et al., 2008; Laukamp et al., 2021, 2011;

423 Portela et al., 2021). Argillic and advanced argillic alteration can be characterised based on the distinctive spectral signature

424 of sulphates, kaolinite, and other clay minerals (Fig. 4). This could be further refined by detailed investigation of the position

425 of these respective absorption features, to distinguish between e.g., kaolinite and dickite or illite and smectite (e.g.,

426 Kereszturi et al., 2020; Simpson and Rae, 2018).

427 Our results also show that the combined depth of v-OH and v+ $\delta$ H-O-H absorptions can be used as a broad but useful proxy

428 for hydrothermal alteration in non-weathered crystallised volcanic rocks, as these lithologies tend to be initially water poor.

429 That said, this index likely cannot identify hydrothermal alteration in tuff units, which can be hydrated during or shortly after

430 formation (e.g., palagonite). Our hydration index shows a weak correlation with physical and mechanical properties (Fig. 5),

431 with substantial unexplained variance that emphasises the important additional influence of microstructure (porosity,

432 grain-size, glass content, and micro-fractures).

#### 434 5.4 Applications and future directions

435 Unlike other commonly applied proxies for physical and mechanical rock properties (e.g., Schmidt hardness, field estimates

436 for porosity, etc.), hyperspectral data can be collected remotely using imaging techniques. This imaging capability unlocks

437 several intriguing possibilities.

433

438 Firstly, our machine learning models could be applied to hyperspectral imagery of hand-sample sized specimens acquired

439 during geotechnical fieldwork to create prior predictions of their physical and mechanical property variability. The locations

440 of extracted mechanical test cores could then be optimized to cover the range of expected variability, improving the

441 statistical representativity of the resulting data. Such an approach would provide an opportunity to independently validate our

442 model predictions, and provide training data for future refinements, while helping ensure statistically representative

443 characterisation of heterogeneous rock masses.

444 Secondly, imaging hyperspectral sensors can also be deployed on tripod, crewed, and uncrewed aircraft to remotely capture

445 ~1 to 10 cm resolution data over large areas of exposed rock. This resolution is comparable to the scale of laboratory tests for

446 physical and mechanical properties, but with a large spatial extent that could enable detailed rock-mass characterisation,

447 through the integration of remotely estimated physical and mechanical property estimates, remotely mapped fracture





448 information (e.g., Dewez et al., 2016; Thiele et al., 2017), and numerical simulation techniques (e.g., Cundall et al., 2008; 449 Ivars et al., 2007). Further development and the acquisition of a larger, more diverse training database is undoubtedly needed 450 before our models can be applied to such "outcrop" settings, due to the lower-quality of hyperspectral data acquired outside 451 of laboratory conditions (where sub-optimal illumination and atmospheric scattering can be problematic) and the variety of 452 weathering processes that can influence outcrop surfaces. However, the required sensors and acquisition techniques already 453 exist, suggesting cm-scale mapping of outcrop physical and mechanical properties is, with appropriate site-specific 454 calibration and validation, achievable.

#### 455 6 Conclusions

456 Our machine learning models demonstrate that hyperspectral data can be used as a proxy for the physical and mechanical 457 properties in the sampled andesitic and basaltic volcanic rocks, with cross validated R2 scores of 0.7 to 0.8. Physical 458 properties, mechanical behaviour, and reflection spectra are influenced by a complex combination of primary and secondary 459 (alteration or weathering) mineralogy, glass content, porosity, grain size, and surface roughness. Disentangling the influence 460 of these properties on spectral reflectance (for complex mixtures; i.e. rocks) remains challenging but our findings 461 demonstrated that machine learning techniques can be used to find informative relationships between spectral and physical 462 and mechanical properties. Further work is required to assess how robust these predictions are, and if they can be generalised 463 or are best applied after site-specific training. We are confident that our results (and other recent work by e.g., Bakun-Mazor 464 et al., 2024; Kereszturi et al., 2023) underpin how hyperspectral data can serve as informative and easy-to-acquire proxy for 465 physical and mechanical properties of volcanic rocks.

467 Table 1: Spectral indices used to spectrally characterize our samples. Absorption features are classified according to the notation 468 of Laukamp et al., (2021), denoting stretching-related absorptions with v and bending-related absorptions with v and were 469 quantified by fitting an asymmetric gaussian to the specified spectral range and recording its amplitude as a measure of 470 absorption depth. This fitting was conducted using hylite (Thiele et al., 2021), and included a hull correction step to remove 471 spectral features broader than the target range.

Short name	Target	Spectral range (nm)	Indicator for	
H <sub>2</sub> O	vOH+δH <sub>2</sub> O	1800–2120	Molecular water in e.g., clay minerals.	
ОН	vOH	1350–1600	Hydroxyl groups in clay minerals and hydroxylated sulfates (kaolinite, alunite, illite, etc).	
Al-OH	$\nu + \delta(Al)$ -OH	2150–2240	Hydroxyl groups in Al-rich phyllosilicate minerals including illite, smectite, kaolinite, etc.	
Mg-OH	$\nu + \delta(Mg)OH$	2280–2330	Hydroxyl groups in Mg-bearing phyllosilicate, like Mg-rich smectites (e.g., hectorite).	
$\mathrm{SO}_4$	δSO	1700–1800	Indicator for the presence of sulfate-bearing minerals,	

vSiO

 $v + \delta M2OHo$ 



Silica

Kaolinite



India	ator for quartz or amorphous silica via the
	nd overtone SiO absorption. This was used
	er than the LWIR feature) to avoid interference
with	plagioclase.

Depth of the  $\nu+\delta(Al)$ -OH related doublet typical of kaolinite group minerals. Note that the hull correction applied prior to fitting removes the influence of the

deeper absorption at 2200 nm.

including gypsum and alunite.

472

473 Table 2: Five-fold cross validated R2 scores for the machine learning approaches trained and tested on: (1) basaltic (MFI < 0.4), (2) 474 andesitic (MFI > 0.4), and (3) combined subsets. The best R2 scores for each property are indicated in bold. The ensemble models 475 were constructed by combining the best-performing SVR and MLP models.

4400-4600

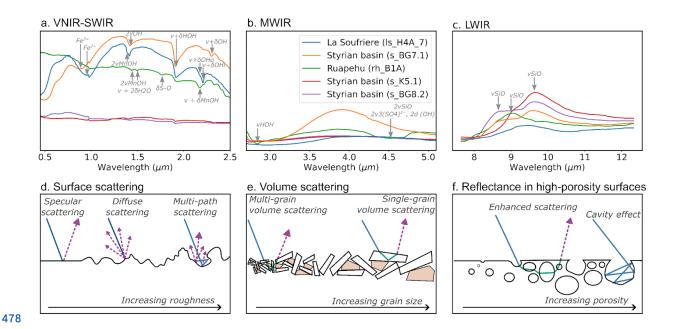
2100-2200

	Lasso	PLSR	SVR	MLP (uni)	MLP (multi)	Ensemble
Density	0.39	0.51	0.76	0.82	0.85	0.84
Density (basalt) Density (andesite)	0.5 0.32	0.47 0.47	0.77 0.79	0.75 <b>0.85</b>	<b>0.83</b> 0.83	0.78 0.84
Porosity	0.33	0.48	0.74	0.79	0.81	0.81
Porosity (basalt) Porosity (andesite)	0.39 0.31	0.49 0.49	0.77 0.74	0.73 0.80	<b>0.81</b> 0.77	0.76 <b>0.80</b>
UCS	0.21	0.18	0.59	0.69	0.66	0.67
UCS (basalt) UCS (andesite)	0.56 0.1	<0	0.76 0.57	0.76 0.67	0.75 0.67	0.75 0.66
E	0.30	0.36	0.65	0.67	0.67	0.70
E (basalt) E (andesite)	0.44 0.31	0.41 0.41	0.68 0.64	0.73 0.62	<b>0.75</b> 0.62	0.73 <b>0.65</b>

476



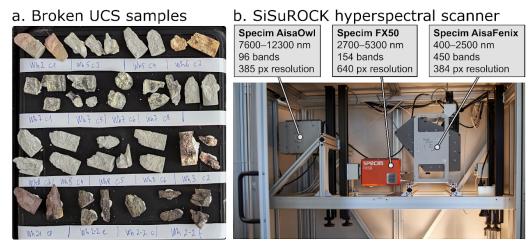


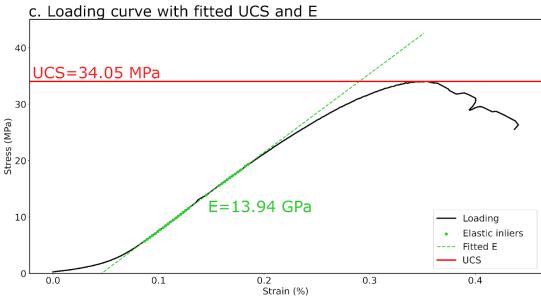


479 Figure. 1: Mineralogical and physical controls on hyperspectral reflectance spectra. Examples of absorption features caused by 480 minerals commonly found in volcanic rocks are shown for the VNIR-SWIR (a), MWIR (b) and LWIR (c) ranges, as described in 481 depth by Laukamp et al., (2021). Typical surface (d) and volume scattering (e) interactions are shown, highlighting the effect of 482 increasing surface roughness and grain size. An example of how these processes operate simultaneously, and are both strongly 483 influenced by porosity, is shown in (f). Note that these are all wavelength dependent, especially where the wavelength of light 484 approaches the scale of variation.





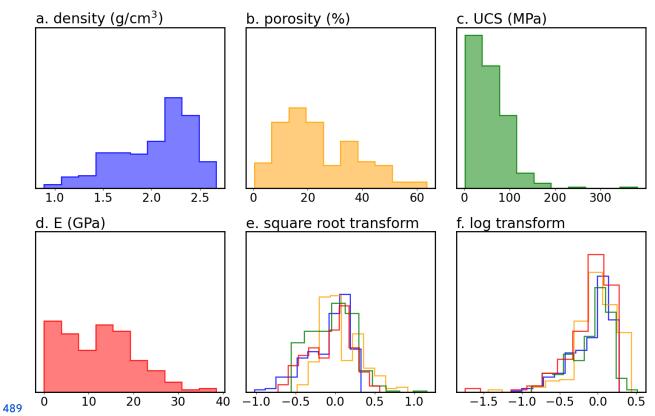




486 Figure. 2: Post-failure uniaxial compressive strength (UCS) test cores (a) prior to scanning in a SiSuROCK hyperspectral drillcore 487 scanner (b). UCS and Young's modulus (E) were extracted from the corresponding stress-strain curves (c) using an automated 488 RANSAC-based procedure, for direct comparison with the (averaged) sample spectra.



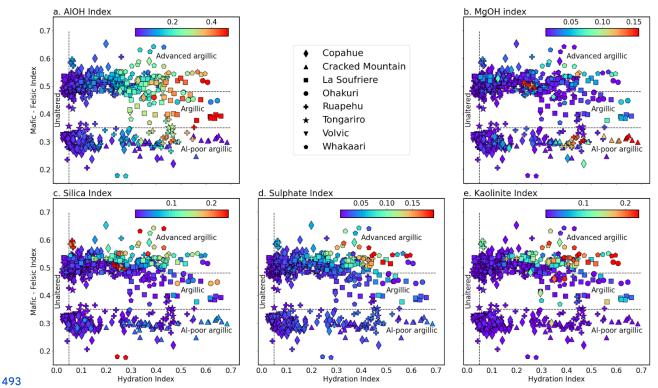




490 Figure. 3: Distributions of the training data before (a-d) and after square root (e) and log (f) transformation. Note that 491 transformed data was normalised to have a median of 0 and 2nd to 98th percentile range of 1. The square root transform (e) 492 resulted in approximately normal distributions.



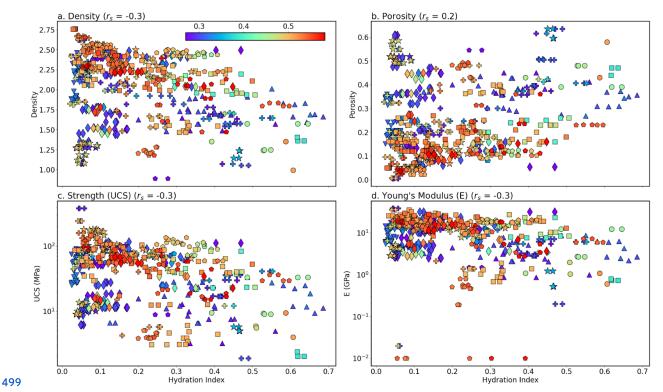




494 Figure. 4: Measured hydration index (x-axis) and Mafic-Felsic Index (MFI; y-axis), coloured by hyperspectral indices for Al-OH 495 bearing phyllosilicates (a), Mg-OH bearing phyllosilicates such as hectorite (b), quartz (c), sulfate (d), and kaolinite (e). The two 496 main clusters indicate the broadly basaltic (lower) or andesitic (upper) composition of the samples, while hydrothermal alteration 497 (and/or surface weathering) results in significant scatter along the x-axis. Distinctive Al-OH and Mg-OH (clay) rich zones indicate 498 argillic alteration, while samples with elevated sulfate and kaolinite indices were likely subject to advanced argillic alteration.







500 Figure. 5: Biplots of our hydration index and density (a), porosity (b), uniaxial compressive strength (UCS) (c) and Young's 501 modulus (E) (d). These indicate that increasing hydration due to hydrothermal alteration and/or weathering tends to decrease 502 density, UCS and E and slightly increase porosity. These trends are (unsurprisingly) quite weak, with Spearman rank correlation 503 coefficients of 0.2–0.3. Colours indicate each sample's MFI, such that basalts are blue and andesites are red. Please refer to the 504 legend of Fig. 3 for the symbols indicating each volcano.





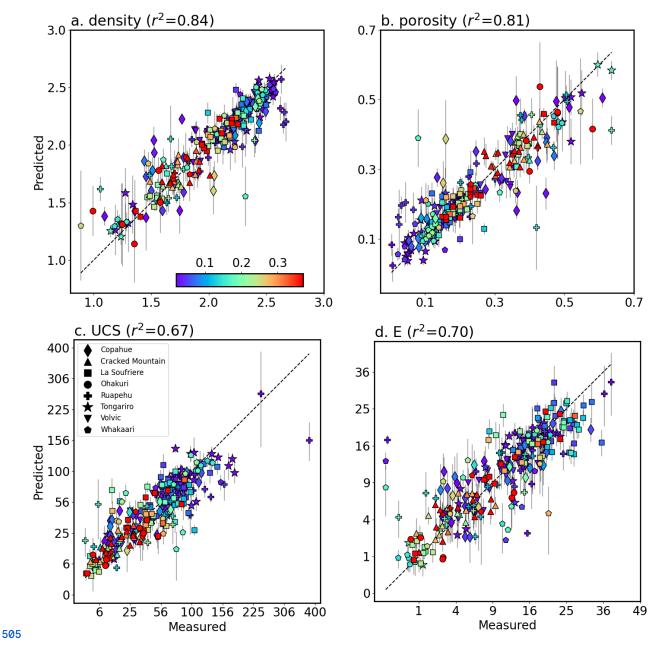
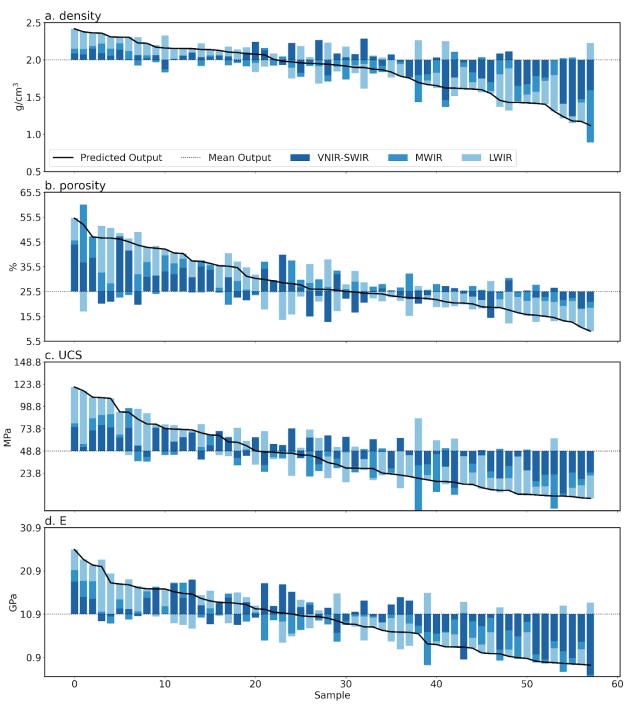


Figure. 6: Five-fold cross validation predictions for density (a), porosity (b), uniaxial compressive strength (UCS) (c) and Young's modulus (E) (d) derived using our ensemble of SVM and multilayer perceptron models. The consistency of the ensemble predictions, quantified as the standard deviation of model predictions, are shown as  $2\sigma$  error bars. The majority of the predictions are thus within error of the measured values, although there are also several notable outliers. Symbols denote the different volcanoes included in the dataset, and colours reflect the hydration index (Fig. 3). Note that the x- and y-axes in (c) and (d) use a square-root scale to better visualise data clustered around lower values of UCS and E.







513 Figure. 7: Shapley values summed for each spectral range (VNIR-SWIR, MWIR, and LWIR) from the joint model (trained on 514 both basalt and andesite) ensemble, indicating the cumulative contribution of each spectral range to predicted density (a), porosity 515 (b), uniaxial compressive strength (UCS) (c) and Young's modulus (E) (d). Values for each property are sorted from high to low 516 predicted value along the x-axis. Higher predictions relative to the mean prediction (dotted line) for density, UCS, and E appear 517 largely driven by LWIR features, while lower values are associated with strong negative contributions from the VNIR-SWIR





518 range. These VNIR-SWIR bands push the predicted value down, and likely indicate the influence of SWIR active hydrated 519 alteration minerals.

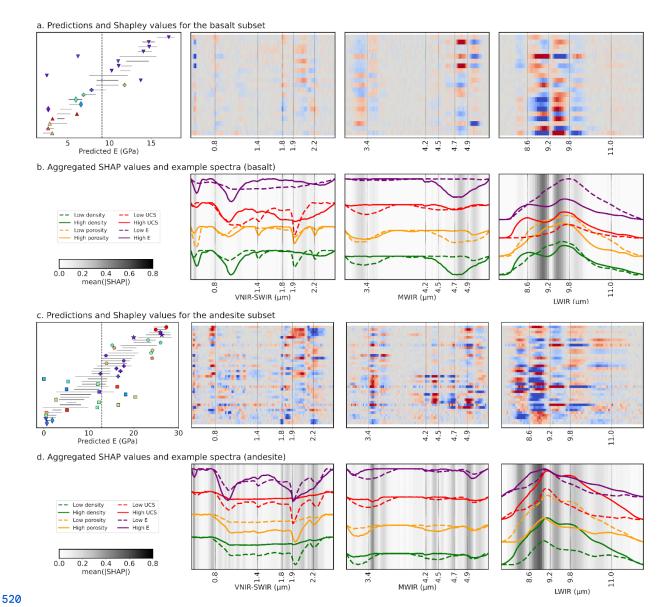


Figure. 8: Shapley values for our predictions of Young's modulus (E) in the basaltic (a, b) and andesitic (c, d) subsets. These were calculated using the ensemble models trained specifically on each subset (to remove aspects of the joint model focused on lithological distinction). Symbols in the left column indicate the measured property values from each volcano (cf. Fig. 3), while the black solid lines show the  $(2\sigma)$  range of values predicted by the ensemble. Deviations of model predictions from the mean (black dashed line) are the sum of the Shapley values along each row, such that blue values indicate bands that decreased the prediction, while red values indicate bands that increased it. Mean absolute SHAP values (b, d), summarising the sensitivity of the model to specific bands are also shown, with spectra from samples with high (solid) and low (dashed) property values for reference. These Shapley values highlight the correspondence of informative bands and inflection points ("shoulders") in the spectra. Shapley value plots for the other mechanical properties can be found in the supplementary information.





## 530 Acknowledgements

531 ST and AK were supported by funding from the European Union's Horizon Europe research and innovation programme 532 under grant agreement no 101058483 and from UK Research and Innovation. GK was supported by the Rutherford 533 Discovery Fellowship of the Royal Society of New Zealand - Te Aparangi ("Caught in action - volcano surveillance with hyperspectral remote sensing"; RDF-MAU2003). MH was supported by ANR grant MYGALE ("Modelling the phYsical 535 and chemical Gradients of hydrothermal ALteration for warning systems of flank collapse at Explosive volcanoes"; 536 ANR-21-CE49-0010) and a European Research Council Synergy Grant (ERC-ROTTnROCK-101118491). MH also 537 acknowledges support from the Institut Universitaire de France (IUF). MRC and MT were supported by the Tellus Program 538 of INSU-CNRS ("Edifice structure and rock strength assessment of Copahue volcano (Argentina/Chile): the role of 539 hyperACidic hydrothermal alteration in VolCano stability (AC/VC))". The hyperspectral sensors used for this study were 540 acquired through funding from the Helmholtz Institute Freiberg for Resource Technology, European Regional Development 541 Fund and the Land of Saxony.

#### **542** References

- 543 Arens, F., Coco, A., Gottsmann, J., Hickey, J., Kilgour, G., 2022. Multiphysics Modeling of Volcanic Unrest at Mt. Ruapehu
- 544 (New Zealand). Geochem. Geophys. Geosystems 23, e2022GC010572. https://doi.org/10.1029/2022GC010572
- 545 Aubry, T.J., Farquharson, J.I., Rowell, C.R., Watt, S.F.L., Pinel, V., Beckett, F., Fasullo, J., Hopcroft, P.O., Pyle, D.M.,
- 546 Schmidt, A., Sykes, J.S., 2022. Impact of climate change on volcanic processes: current understanding and future
- 547 challenges. Bull. Volcanol. 84, 58. https://doi.org/10.1007/s00445-022-01562-8
- 548 Bakun-Mazor, D., Ben-Ari, Y., Marco, S., Ben-Dor, E., 2024. Predicting Mechanical Properties of Carbonate Rocks Using
- 549 Spectroscopy Across 0.4–12 μm. Rock Mech. Rock Eng. 57, 8951–8968. https://doi.org/10.1007/s00603-024-04035-w
- 550 Chandrasekhar, S. (Subrahmanyan), 1960. Radiative transfer. New York: Dover Publications.
- 551 Cudahy, T., Jones, M., Thomas, M., Laukamp, C., Caccetta, M., Hewson, R., Rodger, A., Verrall, M., 2008. Next generation
- mineral mapping: Queensland airborne HyMap and satellite ASTER surveys 2006–2008. Perth Publicly Available Rep.
- **553** P2007364 152.
- 554 Cundall, P.A., Pierce, M.E., Mas Ivars, D., 2008. Quantifying the size effect of rock mass strength, in: SHIRMS 2008:
- 555 Proceedings of the First Southern Hemisphere International Rock Mechanics Symposium. Australian Centre for
- 556 Geomechanics, pp. 3–15.
- 557 del Potro, R., Hürlimann, M., 2009. A Comparison of Different Indirect Techniques to Evaluate Volcanic Intact Rock
- 558 Strength. Rock Mech. Rock Eng. 42, 931–938. https://doi.org/10.1007/s00603-008-0001-5
- 559 Dewez, T.J.B., Girardeau-Montaut, D., Allanic, C., Rohmer, J., 2016. Facets: a cloudcompare plugin to extract geological
- planes from unstructured 3D point clouds. ISPRS Int. Arch. Photogramm. Remote Sens. Spat. Inf. Sci. XLI-B5, 799.
- 561 https://doi.org/10.5194/isprsarchives-xli-b5-799-2016





- 562 Dinçer, I., Acar, A., Çobanoğlu, I., Uras, Y., 2004. Correlation between Schmidt hardness, uniaxial compressive strength and
- 563 Young's modulus for andesites, basalts and tuffs. Bull. Eng. Geol. Environ. 63, 141–148.
- 564 https://doi.org/10.1007/s10064-004-0230-0
- 565 Farquharson, J., Heap, M.J., Varley, N.R., Baud, P., Reuschlé, T., 2015. Permeability and porosity relationships of
- edifice-forming andesites: A combined field and laboratory study. J. Volcanol. Geotherm. Res. 297, 52–68.
- 567 https://doi.org/10.1016/j.jvolgeores.2015.03.016
- 568 Foster, S., Chilton, J., Nijsten, G.-J., Richts, A., 2013. Groundwater—a global focus on the 'local resource.' Curr. Opin.
- 569 Environ. Sustain., Aquatic and marine systems 5, 685–695. https://doi.org/10.1016/j.cosust.2013.10.010
- 570 Franzosi, F., Crippa, C., Derron, M.-H., Jaboyedoff, M., Agliardi, F., 2023. Slope-Scale Remote Mapping of Rock Mass
- 571 Fracturing by Modeling Cooling Trends Derived from Infrared Thermography. Remote Sens. 15, 4525.
- 572 https://doi.org/10.3390/rs15184525
- 573 Griffiths, L., Heap, M.J., Baud, P., Schmittbuhl, J., 2017. Quantification of microcrack characteristics and implications for
- stiffness and strength of granite. Int. J. Rock Mech. Min. Sci. 100, 138–150. https://doi.org/10.1016/j.ijrmms.2017.10.013
- 575 Hapke, B., 2012. Theory of Reflectance and Emittance Spectroscopy. Cambridge University Press.
- 576 Hapke, B., 2008. Bidirectional reflectance spectroscopy: 6. Effects of porosity. Icarus 195, 918–926.
- 577 https://doi.org/10.1016/j.icarus.2008.01.003
- 578 Hapke, B., 2002. Bidirectional Reflectance Spectroscopy: 5. The Coherent Backscatter Opposition Effect and Anisotropic
- 579 Scattering. Icarus 157, 523–534. https://doi.org/10.1006/icar.2002.6853
- 580 Hapke, B., 1993. Theory of Reflectance and Emittance Spectroscopy, Topics in Remote Sensing. Cambridge University
- 581 Press, Cambridge. https://doi.org/10.1017/CBO9780511524998
- 582 Hapke, B., 1986. Bidirectional reflectance spectroscopy: 4. The extinction coefficient and the opposition effect. Icarus 67,
- 583 264–280. https://doi.org/10.1016/0019-1035(86)90108-9
- 584 Hapke, B., 1984. Bidirectional reflectance spectroscopy: 3. Correction for macroscopic roughness. Icarus 59, 41–59.
- 585 https://doi.org/10.1016/0019-1035(84)90054-X
- 586 Hapke, B., 1981. Bidirectional reflectance spectroscopy: 1. Theory. J. Geophys. Res. Solid Earth 86, 3039–3054.
- 587 https://doi.org/10.1029/JB086iB04p03039
- 588 Hardgrove, C.J., Rogers, A.D., Glotch, T.D., Arnold, J.A., 2016. Thermal emission spectroscopy of microcrystalline
- sedimentary phases: Effects of natural surface roughness on spectral feature shape. J. Geophys. Res. Planets 121,
- 590 542–555. https://doi.org/10.1002/2015JE004919
- 591 Harnett, C.E., Heap, M.J., 2021. Mechanical and topographic factors influencing lava dome growth and collapse. J.
- 592 Volcanol. Geotherm. Res. 420, 107398. https://doi.org/10.1016/j.jvolgeores.2021.107398
- 593 Harnett, C.E., Kendrick, J.E., Lamur, A., Thomas, M.E., Stinton, A., Wallace, P.A., Utley, J.E.P., Murphy, W., Neuberg, J.,
- Lavallée, Y., 2019. Evolution of Mechanical Properties of Lava Dome Rocks Across the 1995–2010 Eruption of
- Soufrière Hills Volcano, Montserrat. Front. Earth Sci. 7. https://doi.org/10.3389/feart.2019.00007





- 596 Heap, M.J., Baumann, T., Gilg, H.A., Kolzenburg, S., Ryan, A.G., Villeneuve, M., Russell, J.K., Kennedy, L.A.,
- 897 Rosas-Carbajal, M., Clynne, M.A., 2021a. Hydrothermal alteration can result in pore pressurization and volcano
- instability. Geology 49, 1348–1352. https://doi.org/10.1130/G49063.1
- 599 Heap, M.J., Baumann, T.S., Rosas-Carbajal, M., Komorowski, J.-C., Gilg, H.A., Villeneuve, M., Moretti, R., Baud, P.,
- 600 Carbillet, L., Harnett, C., Reuschlé, T., 2021b. Alteration-Induced Volcano Instability at La Soufrière de Guadeloupe
- 601 (Eastern Caribbean). J. Geophys. Res. Solid Earth 126, e2021JB022514. https://doi.org/10.1029/2021JB022514
- 602 Heap, M.J., Gravley, D.M., Kennedy, B.M., Gilg, H.A., Bertolett, E., Barker, S.L.L., 2020a. Quantifying the role of
- 603 hydrothermal alteration in creating geothermal and epithermal mineral resources: The Ohakuri ignimbrite (Taupō
- 604 Volcanic Zone, New Zealand). J. Volcanol. Geotherm. Res. 390, 106703.
- 605 https://doi.org/10.1016/j.jvolgeores.2019.106703
- 606 Heap, M.J., Troll, V.R., Harris, C., Gilg, H.A., Moretti, R., Rosas-Carbajal, M., Komorowski, J.-C., Baud, P., 2022.
- 607 Whole-rock oxygen isotope ratios as a proxy for the strength and stiffness of hydrothermally altered volcanic rocks. Bull.
- Volcanol. 84, 74. https://doi.org/10.1007/s00445-022-01588-y
- 609 Heap, M.J., Villeneuve, M., Albino, F., Farquharson, J.I., Brothelande, E., Amelung, F., Got, J.-L., Baud, P., 2020b. Towards
- 610 more realistic values of elastic moduli for volcano modelling. J. Volcanol. Geotherm. Res. 390, 106684.
- 611 https://doi.org/10.1016/j.jvolgeores.2019.106684
- 612 Heap, M.J., Violay, M.E.S., 2021. The mechanical behaviour and failure modes of volcanic rocks: a review. Bull. Volcanol.
- 83, 33. https://doi.org/10.1007/s00445-021-01447-2
- 614 Hickey, J., Pascal, K., Head, M., Gottsmann, J., Fournier, N., Hreinsdottir, S., Syers, R., 2022. Magma pressurization
- sustains ongoing eruptive episode at dome-building Soufrière Hills volcano, Montserrat. Geology 50, 1261–1265.
- 616 https://doi.org/10.1130/G50239.1
- 617 Hoek, E., Diederichs, M.S., 2006. Empirical estimation of rock mass modulus. Int. J. Rock Mech. Min. Sci. 43, 203–215.
- 618 Huang, J., Liu, S., Liu, W., Zhang, C., Li, S., Yu, M., Wu, L., 2021. Experimental Study on the Thermal Infrared Spectral
- Variation of Fractured Rock. Remote Sens. 13, 1191. https://doi.org/10.3390/rs13061191
- 620 Hunt, G.R., Vincent, R.K., 1968. The behavior of spectral features in the infrared emission from particulate surfaces of
- 621 various grain sizes. J. Geophys. Res. 1896-1977 73, 6039–6046. https://doi.org/10.1029/JB073i018p06039
- 622 Ivars, D.M., Deisman, N., Pierce, M., Fairhurst, C., 2007. The synthetic rock mass approach-a step forward in the
- characterization of jointed rock masses, in: 11th ISRM Congress. OnePetro.
- 624 Kereszturi, G., Heap, M., Schaefer, L.N., Darmawan, H., Deegan, F.M., Kennedy, B., Komorowski, J.-C., Mead, S.,
- Rosas-Carbajal, M., Ryan, A., Troll, V.R., Villeneuve, M., Walter, T.R., 2023. Porosity, strength, and alteration Towards
- a new volcano stability assessment tool using VNIR-SWIR reflectance spectroscopy. Earth Planet. Sci. Lett. 602, 117929.
- 627 https://doi.org/10.1016/j.epsl.2022.117929





- 628 Kereszturi, G., Schaefer, L.N., Miller, C., Mead, S., 2020. Hydrothermal Alteration on Composite Volcanoes: Mineralogy,
- 629 Hyperspectral Imaging, and Aeromagnetic Study of Mt Ruapehu, New Zealand. Geochem. Geophys. Geosystems 21,
- e2020GC009270. https://doi.org/10.1029/2020GC009270
- 631 Kidd, M., Kereszturi, G., Kennedy, B., Heap, M., Procter, J., 2025. Linking hydrothermal alteration to rock mechanics:
- comparative analysis of andesitic volcanoes in Aotearoa New Zealand.
- 633 Kirkland, L.E., Herr, K.C., Adams, P.M., 2003. Infrared stealthy surfaces: Why TES and THEMIS may miss some
- substantial mineral deposits on Mars and implications for remote sensing of planetary surfaces. J. Geophys. Res. Planets
- 635 108. https://doi.org/10.1029/2003JE002105
- 636 Kirkland, L.E., Herr, K.C., Salisbury, J.W., 2001. Thermal infrared spectral band detection limits for unidentified surface
- 637 materials. Appl. Opt. 40, 4852–4862. https://doi.org/10.1364/AO.40.004852
- 638 Laukamp, C., Cudahy, T., Cleverley, J.S., Oliver, N.H.S., Hewson, R., 2011. Airborne hyperspectral imaging of
- 639 hydrothermal alteration zones in granitoids of the Eastern Fold Belt, Mount Isa Inlier, Australia. Geochem. Explor.
- 640 Environ. Anal. 11, 3–24. https://doi.org/10.1144/1467-7873/09-231
- 641 Laukamp, C., Rodger, A., LeGras, M., Lampinen, H., Lau, I.C., Pejcic, B., Stromberg, J., Francis, N., Ramanaidou, E., 2021.
- 642 Mineral Physicochemistry Underlying Feature-Based Extraction of Mineral Abundance and Composition from
- Shortwave, Mid and Thermal Infrared Reflectance Spectra. Minerals 11, 347. https://doi.org/10.3390/min11040347
- 644 Lee, J., Cook, O.J., Argüelles, A.P., Mehmani, Y., 2023. Imaging geomechanical properties of shales with infrared light. Fuel
- 334, 126467. https://doi.org/10.1016/j.fuel.2022.126467
- 646 Leight, C.J., Ytsma, C., McCanta, M.C., Dyar, M.D., Glotch, T.D., 2024. Compositional Characterization of Glassy Volcanic
- 647 Material From VSWIR and MIR Spectra Using Partial Least Squares Regression Models. Earth Space Sci. 11,
- e2023EA003439. https://doi.org/10.1029/2023EA003439
- 649 Leiter, S., Russell, J.K., Heap, M.J., Barendregt, R.W., Wilson, S., Edwards, B., 2024. Distribution, intensity, and timing of
- 650 palagonitization in glaciovolcanic deposits, Cracked Mountain volcano, Canada. Bull. Volcanol. 86, 32.
- 651 https://doi.org/10.1007/s00445-024-01724-w
- 652 Lewicka, E., Guzik, K., Galos, K., 2021. On the Possibilities of Critical Raw Materials Production from the EU's Primary
- 653 Sources. Resources 10, 50. https://doi.org/10.3390/resources10050050
- 654 Loche, M., Scaringi, G., Blahůt, J., Melis, M.T., Funedda, A., Da Pelo, S., Erbì, I., Deiana, G., Meloni, M.A., Cocco, F.,
- 655 2021. An Infrared Thermography Approach to Evaluate the Strength of a Rock Cliff. Remote Sens. 13, 1265.
- 656 https://doi.org/10.3390/rs13071265
- 657 Lund, J.W., Toth, A.N., 2021. Direct utilization of geothermal energy 2020 worldwide review. Geothermics 90, 101915.
- 658 https://doi.org/10.1016/j.geothermics.2020.101915
- 659 Lundberg, S., Lee, S.-I., 2017. A Unified Approach to Interpreting Model Predictions.
- 660 https://doi.org/10.48550/arXiv.1705.07874





- 661 Lyon, R.J.P., 1965. Analysis of rocks by spectral infrared emission (8 to 25 microns). Econ. Geol. 60, 715-736.
- 662 https://doi.org/10.2113/gsecongeo.60.4.715
- 663 Mineo, S., Pappalardo, G., 2016. The Use of Infrared Thermography for Porosity Assessment of Intact Rock. Rock Mech.
- Rock Eng. 49, 3027–3039. https://doi.org/10.1007/s00603-016-0992-2
- 665 Mordensky, S.P., Villeneuve, M.C., Farquharson, J.I., Kennedy, B.M., Heap, M.J., Gravley, D.M., 2018. Rock mass
- properties and edifice strength data from Pinnacle Ridge, Mt. Ruapehu, New Zealand. J. Volcanol. Geotherm. Res. 367,
- 46–62. https://doi.org/10.1016/j.jvolgeores.2018.09.012
- 668 Mustard, J.F., Hays, J.E., 1997. Effects of Hyperfine Particles on Reflectance Spectra from 0.3 to 25 µm. Icarus 125,
- 669 145–163. https://doi.org/10.1006/icar.1996.5583
- 670 Osterloo, M.M., Hamilton, V.E., Anderson, F.S., 2012. A laboratory study of the effects of roughness on the thermal infrared
- 671 spectra of rock surfaces. Icarus 220, 404–426. https://doi.org/10.1016/j.icarus.2012.04.020
- 672 Poganj, A., Heap, M.J., Baud, P., 2025. Spatial distribution of alteration and strength in a lava dome: Implications for
- large-scale volcano stability modelling. J. Volcanol. Geotherm. Res.
- 674 Pola, A., Crosta, G., Fusi, N., Barberini, V., Norini, G., 2012. Influence of alteration on physical properties of volcanic rocks.
- 675 Tectonophysics 566–567, 67–86. https://doi.org/10.1016/j.tecto.2012.07.017
- 676 Portela, B., Sepp, M.D., van Ruitenbeek, F.J.A., Hecker, C., Dilles, J.H., 2021. Using hyperspectral imagery for
- 677 identification of pyrophyllite-muscovite intergrowths and alunite in the shallow epithermal environment of the Yerington
- 678 porphyry copper district. Ore Geol. Rev. 131, 104012. https://doi.org/10.1016/j.oregeorev.2021.104012
- 679 Rost, E., Hecker, C., Schodlok, M.C., Van der Meer, F.D., 2018. Rock Sample Surface Preparation Influences Thermal
- 680 Infrared Spectra. Minerals 8, 475. https://doi.org/10.3390/min8110475
- 681 Salisbury, J.W., Eastes, J.W., 1985. The effect of particle size and porosity on spectral contrast in the mid-infrared. Icarus 64,
- 586–588. https://doi.org/10.1016/0019-1035(85)90078-8
- 683 Salisbury, J.W., Wald, A., 1992. The role of volume scattering in reducing spectral contrast of reststrahlen bands in spectra of
- 684 powdered minerals. Icarus 96, 121–128. https://doi.org/10.1016/0019-1035(92)90009-V
- 685 Schaefer, L.N., Kereszturi, G., Kennedy, B.M., Villeneuve, M., 2023. Characterizing lithological, weathering, and
- 686 hydrothermal alteration influences on volcanic rock properties via spectroscopy and laboratory testing: a case study of
- 687 Mount Ruapehu volcano, New Zealand. Bull. Volcanol. 85, 43. https://doi.org/10.1007/s00445-023-01657-w
- 688 Schaefer, L.N., Kereszturi, G., Villeneuve, M., Kennedy, B., 2021. Determining physical and mechanical volcanic rock
- 689 properties via reflectance spectroscopy. J. Volcanol. Geotherm. Res. 420, 107393.
- 690 https://doi.org/10.1016/j.jvolgeores.2021.107393
- 691 Schodlok, M.C., Whitbourn, L., Huntington, J., Mason, P., Green, A., Berman, M., Coward, D., Connor, P., Wright, W.,
- Jolivet, M., Martinez, R., 2016. HyLogger-3, a visible to shortwave and thermal infrared reflectance spectrometer system
- for drill core logging: functional description. Aust. J. Earth Sci.





- 694 Shapley, L.S., 1973. On Balanced Games without Side Payments, in: Hu, T.C., Robinson, S.M. (Eds.), Mathematical
- 695 Programming, Academic Press, pp. 261–290. https://doi.org/10.1016/B978-0-12-358350-5.50012-9
- 696 Simpson, M.P., Rae, A.J., 2018. Short-wave infrared (SWIR) reflectance spectrometric characterisation of clays from
- 697 geothermal systems of the Taupō Volcanic Zone, New Zealand. Geothermics 73, 74–90.
- 698 https://doi.org/10.1016/j.geothermics.2018.01.006
- 699 Soltani, M., Moradi Kashkooli, F., Dehghani-Sanij, A.R., Nokhosteen, A., Ahmadi-Joughi, A., Gharali, K., Mahbaz, S.B.,
- 700 Dusseault, M.B., 2019. A comprehensive review of geothermal energy evolution and development. Int. J. Green Energy
- 701 16, 971–1009. https://doi.org/10.1080/15435075.2019.1650047
- 702 Strehlow, K., Gottsmann, J.H., Rust, A.C., 2015. Poroelastic responses of confined aquifers to subsurface strain and their use
- 703 for volcano monitoring. Solid Earth 6, 1207–1229. https://doi.org/10.5194/se-6-1207-2015
- 704 Swanson, E., Wilson, J., Broome, S., Sussman, A., 2020. The Complicated Link Between Material Properties and
- 705 Microfracture Density for an Underground Explosion in Granite. J. Geophys. Res. Solid Earth 125, e2020JB019894.
- 706 https://doi.org/10.1029/2020JB019894
- 707 Takemura, T., Golshani, A., Oda, M., Suzuki, K., 2003. Preferred orientations of open microcracks in granite and their
- 708 relation with anisotropic elasticity. Int. J. Rock Mech. Min. Sci. 40, 443-454.
- 709 https://doi.org/10.1016/S1365-1609(03)00014-5
- 710 Thiele, S.T., Bnoulkacem, Z., Lorenz, S., Bordenave, A., Menegoni, N., Madriz, Y., Dujoncquoy, E., Gloaguen, R., Kenter,
- 711 J., 2022. Mineralogical Mapping with Accurately Corrected Shortwave Infrared Hyperspectral Data Acquired Obliquely
- 712 from UAVs. Remote Sens. 14, 5. https://doi.org/10.3390/rs14010005
- 713 Thiele, S.T., Grose, L., Samsu, A., Micklethwaite, S., Vollgger, S.A., Cruden, A.R., 2017. Rapid, semi-automatic fracture
- and contact mapping for point clouds, images and geophysical data. Solid Earth 8, 1241.
- 715 Thiele, S.T., Kirsch, M., Lorenz, S., Saffi, H., El Alami, S., Contreras Acosta, I.C., Madriz, Y., Gloaguen, R., 2024.
- 716 Maximising the value of hyperspectral drill core scanning through real-time processing and analysis. Front. Earth Sci. 12.
- 717 https://doi.org/10.3389/feart.2024.1433662
- 718 Thiele, S.T., Lorenz, S., Kirsch, M., Acosta, I.C.C., Tusa, L., Hermann, E., Möckel, R., Gloaguen, R., 2021. Multi-scale,
- 719 multi-sensor data integration for automated 3-D geological mapping using hylite. Ore Geol. Rev. 136.
- 720 https://doi.org/10.1016/j.oregeorev.2021.104252
- 721 Tramontini, M., Rosas-Carbajal, M., Heap, M.J., Besson, P., Marteau, J., García, S., Zyserman, F.I., 2025. The effects of
- hydrothermal alteration in the upper edifice of Copahue volcano (Argentina-Chile). Presented at the IAVCEI Conference,
- 723 Geneva.
- 724 Vairé, E., Heap, M.J., Baud, P., van Wyk de Vries, B., 2024. Quantifying the physical and mechanical heterogeneity of
- 725 porous volcanic rocks from the Chaîne des Puys (Massif Central, France). Bull. Volcanol. 86, 49.
- 726 https://doi.org/10.1007/s00445-024-01742-8





- 727 van der Meer, F., Kopačková, V., Koucká, L., van der Werff, H.M.A., van Ruitenbeek, F.J.A., Bakker, W.H., 2018.
- Wavelength feature mapping as a proxy to mineral chemistry for investigating geologic systems: An example from the
- 729 Rodalquilar epithermal system. Int. J. Appl. Earth Obs. Geoinformation 64, 237–248.
- 730 https://doi.org/10.1016/j.jag.2017.09.008
- 731 Vincent, R.K., Hunt, G.R., 1968. Infrared Reflectance from Mat Surfaces. Appl. Opt. 7, 53-59.
- 732 https://doi.org/10.1364/AO.7.000053
- 733 Vrakas, A., Dong, W., Anagnostou, G., 2018. Elastic deformation modulus for estimating convergence when tunnelling
- through squeezing ground. Géotechnique 68, 713–728. https://doi.org/10.1680/jgeot.17.P.008
- 735 Williams, D.B., Ramsey, M.S., 2024. Infrared spectroscopy of volcanoes: from laboratory to orbital scale. Front. Earth Sci.
- 736 12. https://doi.org/10.3389/feart.2024.1308103